R-03-04

Groundwater flow and transport modelling during a glaciation period

O Jaquet, P Siegel
Colenco Power Engineering Ltd

January 2003

Svensk Kärnbränslehantering AB
Swedish Nuclear Fuel
and Waste Management Co
Box 5864
SE-102 40 Stockholm Sweden
Tel 08-459 84 00
+46 8 459 84 00
Fax 08-661 57 19
+46 8 661 57 19

ISSN 1402-3091
SKB Rapport R-03-04

Groundwater flow and transport modelling during a glaciation period

O Jaquet, P Siegel
Colenco Power Engineering Ltd

January 2003

Content

1 Introduction

Subsequent to work performed by /Svensson, 1999/, SKB has decided to carry out additional hydrogeological modelling studies related to glaciation effects at Äspö. In particular, subglacial groundwater flow and the impact assessment on a repository require further studies. As compared to the previous model /Svensson, 1999/, the domain geometry and processes involved remain identical, but this time, numerical calculations are performed with the NAMMU package (version 7.1.1) using a finite element formulation. Modified assumptions corresponding to specific boundary conditions are implemented and additional variations of the base case are simulated.

2 Objectives

The objectives of the study are based on the technical specifications established by SKB /Selroos, 2001/. The main objectives may be summarised as follows:

- Enhancement of the understanding of subglacial groundwater flow due to basal ice melting.
- Evaluation of the impact of subglacial groundwater flow on a repository with respect to its position to the ice margin of the glacier.
- Assessment of the feasibility of performing large 3D simulations of density-driven flow induced by variable salinity of the groundwater using the NAMMU package.

The report begins with an account of the modelling approach applied. Then, the results of the different cases simulated are described, analysed and interpreted in detail. Finally, conclusions are drawn up together with some recommendations related to potential modelling issues for the future.

3 Modelling approach

The modelling approach is discussed in terms of phenomenology, parameters and boundary conditions considered. Information on the current understanding and conceptualisation of groundwater flow beneath ice sheets was provided by SKB (taken from /Boulton et al, 2001/, and /Vidstrand, 2001/). The foundation of this study relies on previous work performed by /Svensson, 1999/.

3.1 Location and dimension

The computational domain selected for the model corresponds to the one applied by /Svensson, 1999/ for the numerical calculations of subglacial groundwater flow at Äspö (cf Figure 1).

The ice margin is placed right on Äspö with SW-NE orientation (see Figure 2). The model is configured in three dimensions. The size of the domain (see Figure 3) is 250 × 10 × 4 km^3 (length × width × depth).

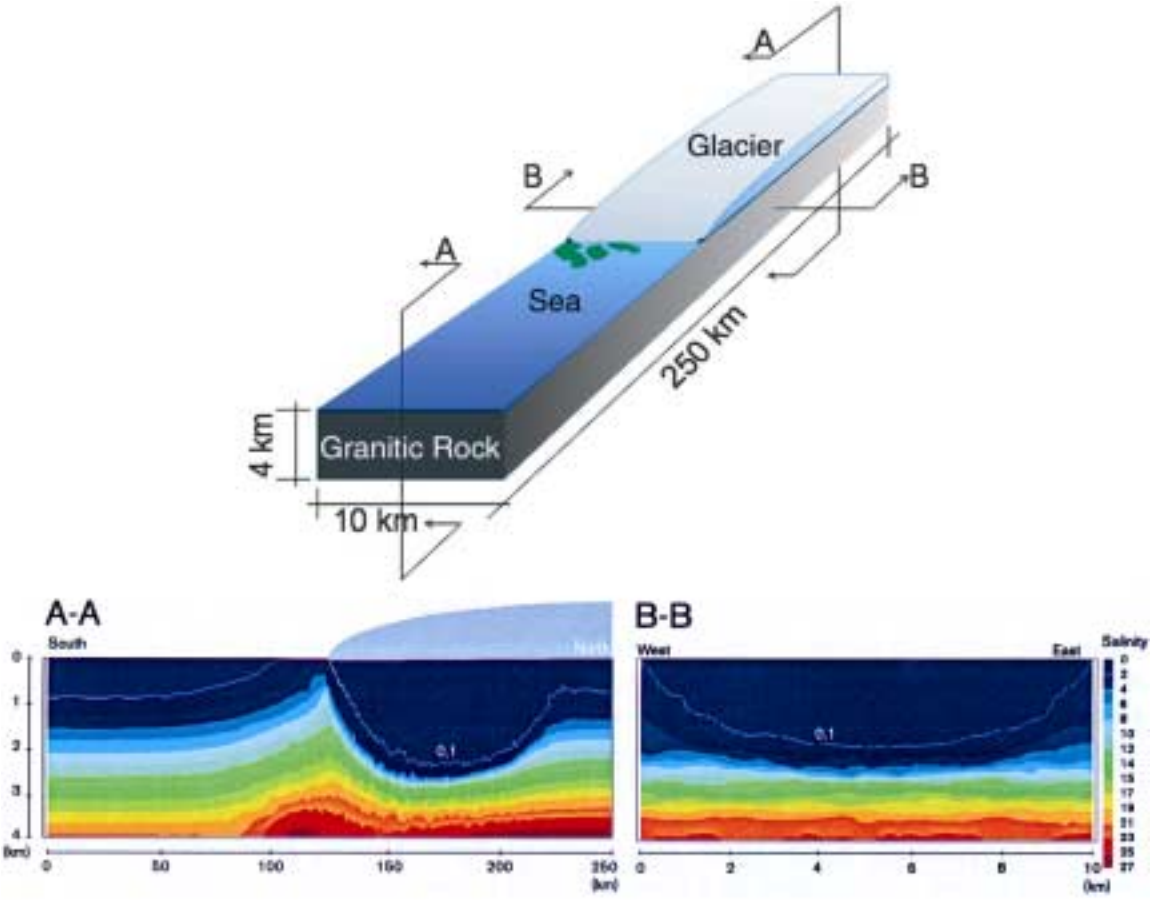

Figure 1 Model of /Svensson, 1999/: domain considered and salinity cross-sections A-A and B-B at 1000 years (taken from /SR 97, 1999/).

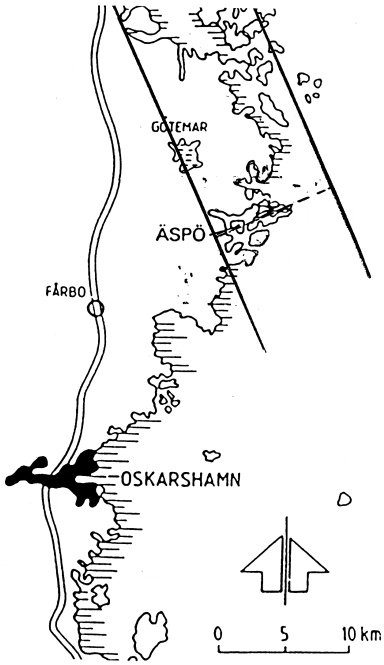

Figure 2 Schematic map of the Äspö region. Thick lines mark eskers (i.e. sedimentary deposits linked to former ice tunnels), the broken line corresponds to the ice margin (taken from /Svensson, 1999/).

3.2 Glacial structures

The ice-front is assumed to have a length of 100 km and a maximum thickness of 1 km. Two ice tunnels are positioned along the edges of the domain. These tunnels are located in the top z-layer, along the y-direction of the domain (co-ordinate directions according to Figure 3), starting at the ice margin, and extending to a distance of 100 km. The width of the ice tunnels is set to approximately 5 m.

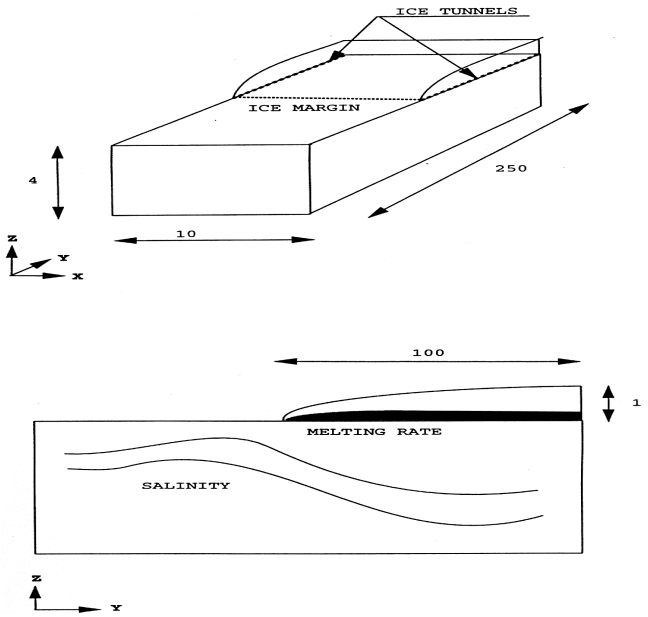

Figure 3 Model extent, distances expressed in kilometres (taken from /Svensson, 1999/).

3.3 Fracture zones

Five major fracture zones are considered (SFZ 02, 05, 10, 12, 15). Their locations were taken from /Rhén et al, 1997/. The major fracture zones were extended to the model boundaries according to the previous modelling study (see Figures 4a and 4b). The major fracture zones are assumed to be vertical and to intersect the entire thickness of the domain.

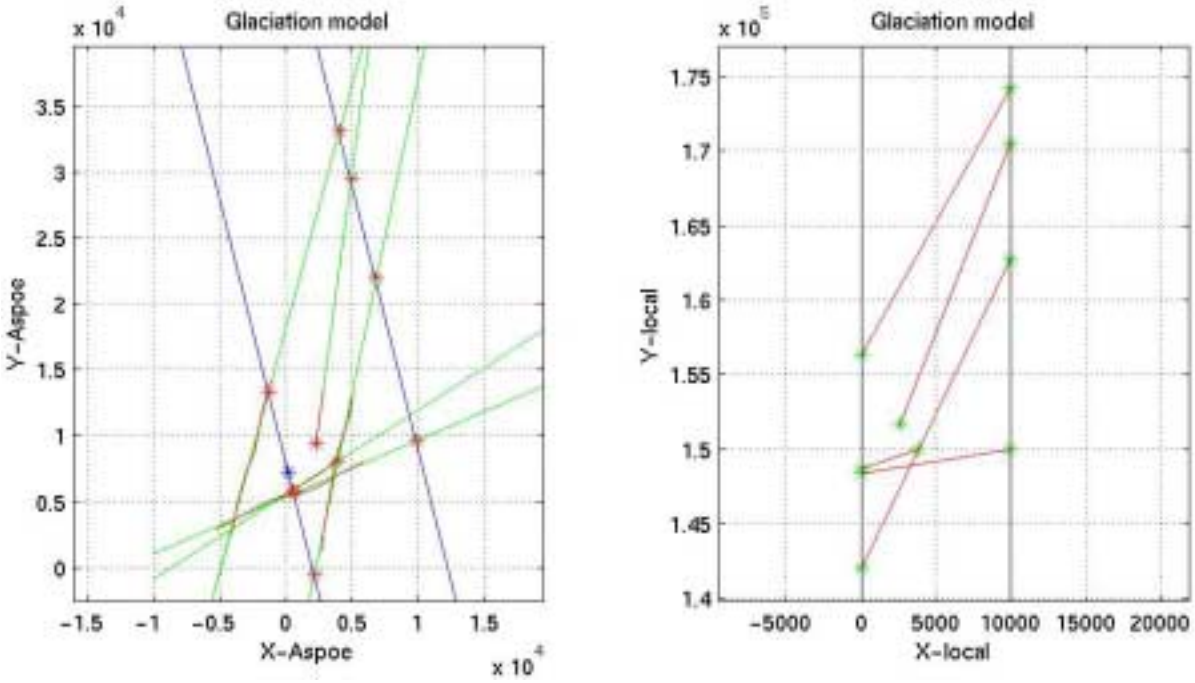

Figure 4a Location of major fracture zones in the Äspö co-ordinate system (left figure: markings in red indicate actual geological observations) and local co-ordinate system of the model (right figure).

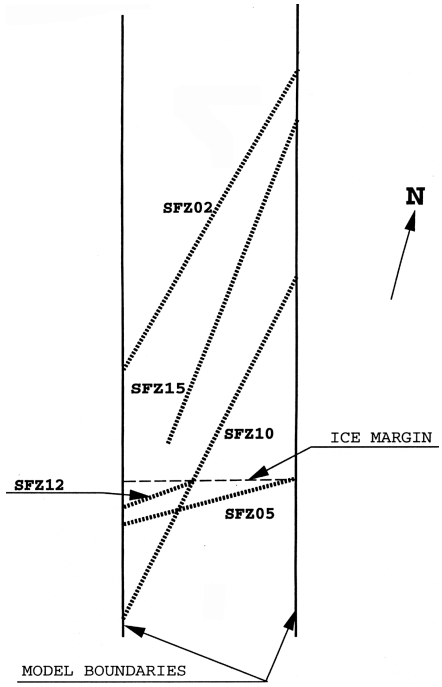

Figure 4b Model position of major fracture zones (taken from /Svensson, 1999/).

3.4 Phenomenology

The description of the density-driven flow induced by the variable salinity of the groundwater requires flow and transport equations. The following forms, fully coupled /Cliffe et al, 1998/, are implemented in NAMMU (version 7.1.1).

The flow equations are governed by Darcy's law:

$$\mathbf{q} = -\frac{\mathbf{k}}{\mu}\left(\nabla p^R - (\rho - \rho_0)\mathbf{g}\right) \quad (1)$$

where:

q = Darcy velocity

k = intrinsic permeability tensor

μ = fluid viscosity

p^R = residual pressure with $p^R = p + \rho_0 g(z - z_0)$

p = pressure

ρ = fluid density

ρ_0 = reference density of fluid

z = elevation

z_0 = reference elevation

g = gravitational acceleration

and the continuity equation:

$$\frac{\partial}{\partial t}(\phi\rho) + \nabla \cdot (\rho\mathbf{q}) = 0 \quad (2)$$

where:

ϕ = porosity

Using the specific storage coefficient:

$$S = \rho g\left(\frac{\partial \phi}{\partial p} + \alpha\phi\right) \quad (3)$$

where:

S = specific storage coefficient

α = fluid compressibility

the continuity equation (2) becomes:

$$\frac{S}{g}\frac{\partial p^R}{\partial t} + \nabla \cdot (\rho \mathbf{q}) + \phi \frac{\partial \rho}{\partial c}\frac{\partial c}{\partial t} = 0 \qquad (4)$$

where:

c = concentration of solute as a mass fraction of the reference concentration

In order to assume quasi steady-state flow conditions, the storage coefficient is set equal to zero, thus simplifying the continuity equation to:

$$\nabla \cdot (\rho \mathbf{q}) + \phi \frac{\partial \rho}{\partial c}\frac{\partial c}{\partial t} = 0 \qquad (5)$$

Regarding salt transport, the advection-dispersion equation applies:

$$\frac{\partial}{\partial t}(\phi \rho c) + \nabla \cdot (\rho \mathbf{q} c) = \nabla \cdot (\phi \rho \mathbf{D} \cdot \nabla c) \qquad (6)$$

where:

D = hydrodynamic dispersion tensor

The hydrodynamic dispersion tensor is defined as follows:

$$\mathbf{D} = \frac{D_m}{\tau}\delta_{ij} + \alpha_T v \delta_{ij} + (\alpha_L - \alpha_T)\frac{v_i v_j}{v} \qquad (7)$$

where:

D_m = molecular diffusion coefficient

τ = tortuosity

α_T, α_L = transverse dispersivity and longitudinal dispersivity

v = porewater velocity (with $\mathbf{v} = \frac{\mathbf{q}}{\phi}$ and $v = \sqrt{\mathbf{v} \cdot \mathbf{v}}$)

The dependence of density upon the solute concentration is given by the following equation of state:

$$\rho = \left(\frac{1 - c}{\rho_0} + \frac{c}{\rho_s} \right)^{-1} \qquad (8)$$

where:

ρ_s = saturation density of the fluid

According to /Svensson, 2002b/, the governing equations (1), (5) and (6), which account for the physical processes, are identical to the ones applied in the previous modelling study /Svensson, 1999/.

3.5 Flow parameters

The spatial variability of the hydraulic properties of the rock mass and the major fracture zones at Äspö was characterised by /Rhén et al, 1997/. The rock mass was divided into four hydrogeological units for which statistical parameters are available (cf Table 1). The hydraulic conductivity is assumed to follow a log-normal distribution (i.e. the log-conductivity distribution is Gaussian). The isotropic correlation scale (i.e. the parameter of the variogram) was estimated using experimental variogram calculations performed for the regional scale.

For this modelling study, the correlation scale is assumed to remain constant for the four hydrogeological units considered.

Table 1 Rock mass hydraulic parameters /after Rhén et al, 1997/.

Depth	Geometric mean of hydraulic conductivity[1)]	Standard deviation	Correlation scale
[m]	[m/s] (scale of hydraulic test in m)	[log 10]	[m]
0–200	$1.3 \cdot 10^{-7}$ (100)	0.96	275[2)]
200–400	$2.0 \cdot 10^{-7}$ (100)	0.65	275
400–600	$2.6 \cdot 10^{-7}$ (100)	0.79	275
600–2000[3)]	$4.7 \cdot 10^{-8}$ (300)	0.72	275

1) Equal to the mean of the log-conductivity values.
2) Corresponds to the practical range of 825 m; cf Figure 6-25 of /Rhén et al, 1997/.
3) In the model these statistical parameters are assumed valid from 600 to 4000 m depth.

A Gaussian random function model with an exponential variogram was then selected for the stochastic representation of the spatial variability of the rock-mass log-conductivity.

The porosity is calculated from the hydraulic conductivity using the following equation /Rhén et al, 1997/:

$$\phi = 34.87\, K^{0.753} \quad \text{with } \phi \leq 0.05 \tag{9}$$

where:

K = hydraulic conductivity

Porosity is spatially variable and correlated to the hydraulic conductivity, no distinction is made between total porosity and effective porosity within the framework of this study.

Due to the limited amount of data available, the transmissivity of the major fracture zones was considered to be constant (cf Table 2).

Table 2 Major fracture zone hydraulic parameters /after Rhén et al, 1997/.

Major fracture zone	Average width [m]	Hydraulic conductivity [m/s]	Transmissivity [m^2/s]	Porosity[1)] [–]
SFZ02	200	$5.0 \cdot 10^{-7}$	10^{-4}	$6.3 \cdot 10^{-4}$
SFZ05	125	$8.0 \cdot 10^{-7}$	10^{-4}	$8.9 \cdot 10^{-4}$
SFZ10	175	$5.7 \cdot 10^{-7}$	10^{-4}	$6.9 \cdot 10^{-4}$
SFZ12	75	$1.3 \cdot 10^{-6}$	10^{-4}	$1.3 \cdot 10^{-3}$
SFZ15	75	$1.3 \cdot 10^{-6}$	10^{-4}	$1.3 \cdot 10^{-3}$

1) Calculated using equation (9)

The fracture zones are implicitly defined as deterministic features using the IFZ method (Implicit Fracture Zone method implemented in NAMMU; /Marsic et al, 2001/). The fracture zones are integrated into the “stochastic” rock mass to obtain equivalent hydraulic properties; i.e. equivalent hydraulic conductivity and porosity are calculated for the mesh elements in order to account for the hydraulic effects of the fracture zones that intercept them.

3.6 Transport parameters

The hydrodynamic dispersion is applied as the following tensor:

$$\mathbf{D} = \begin{vmatrix} D_{xx} & D_{xy} & D_{xz} \\ D_{xy} & D_{yy} & D_{yz} \\ D_{xz} & D_{yz} & D_{zz} \end{vmatrix} \tag{10}$$

where:

D_{xx}, D_{yy}, D_{zz} = principal components

D_{xy}, D_{xz}, D_{yz} = cross terms

The parameters from Table 3 are used for the calculation of the components with equation (7). They were selected based on discussions with SKB and on previous studies in granitic rock formations.

Table 3 Transport parameters.

Transverse dispersivity [m]	Longitudinal dispersivity [m]	Molecular diffusion coefficient [m^2/s]
50	100	$3 \cdot 10^{-9}$

3.7 Discretisation

The spatial discretisation is selected based on the previous study by /Svensson, 1999/ and with the aim of satisfying the transport numerical criterion (i.e. with a numerical Peclet number < 2); at least in the immediate vicinity of the ice margin where large salinity variations are expected.

The discretisation of the numerical model is performed using a finite-element mesh with cuboid elements (8 nodes) of non-uniform size (see Figure 5). The following grid spacing is applied:

- In the **x-direction**: 5, 195, 200, 200, ..., 200, 195, 5 m, where the lateral spacing of 5 m corresponds to the ice tunnels' discretisation.
- In the **y-direction**: along the ice margin, the grid spacing used is 200 m; beyond the ice margin, it increases in size in the North and South directions.
- In the **z-direction**: the following sequence is used for the top 200 m: 10, 10, 10, 10, 10, 20, 30, 40 and 60 m. Below the depth of 200 m, a uniform grid spacing of 100 m is applied.

The resulting mesh contains a total number of 491416 nodes and 467532 elements. Every element of the mesh discretising the rock mass is assigned a hydraulic conductivity and a porosity value obtained from the stochastic simulation (cf section 4.1).

Strictly speaking, the statistical parameters of the hydraulic conductivity are valid for a given scale at which hydraulic testing was performed in the boreholes. In this study, in order to avoid unrealistic computing time for the numerical computation, a regular grid spacing corresponding approximately to the measurement scale was assigned only for the vicinity of the ice margin. The effect of this approximation on the modelling results remains to be answered.

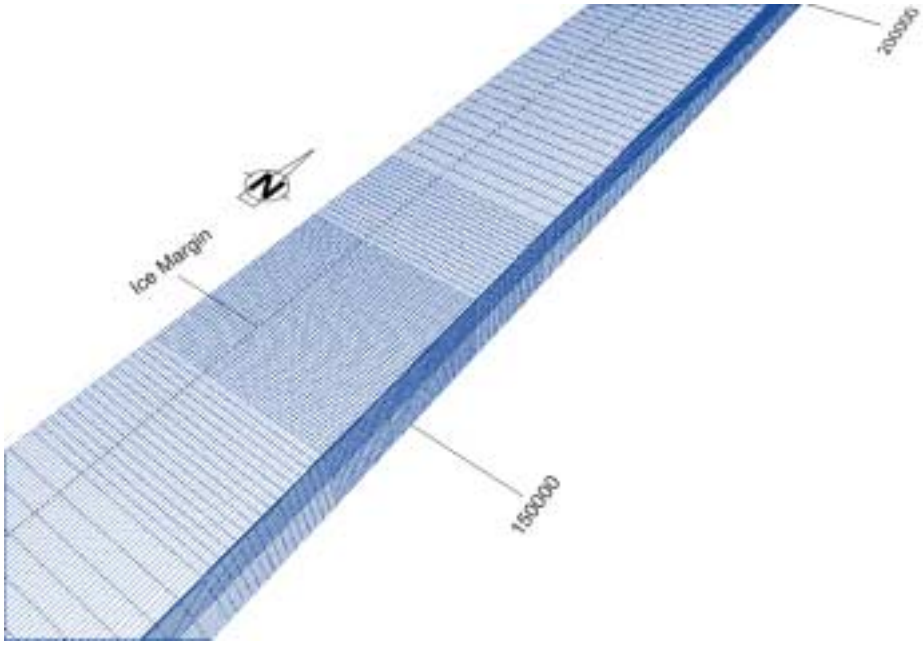

Figure 5 Finite-element mesh.

3.8 Boundary conditions

The flow boundary conditions are the following (see Figure 6):

- **Surface of the model**:
  - North of the ice margin (melting zone with an extent of 100 km): a constant flow is prescribed with a melting rate equal to 50 mm/a.
  - South of the ice margin (remaining 150 km): a pressure equal to zero is prescribed.
- **Lateral and bottom boundaries**: no flow conditions are prescribed.

The salt boundary conditions are taken as follows (see Figure 6):

- **Surface of the model**:
  - North of the ice margin: the concentration of the water infiltrating from the melting zone is set to zero.
  - South of the ice margin: no dispersive flux conditions are prescribed.
- **Lateral and bottom boundaries**: no dispersive flux conditions are prescribed.

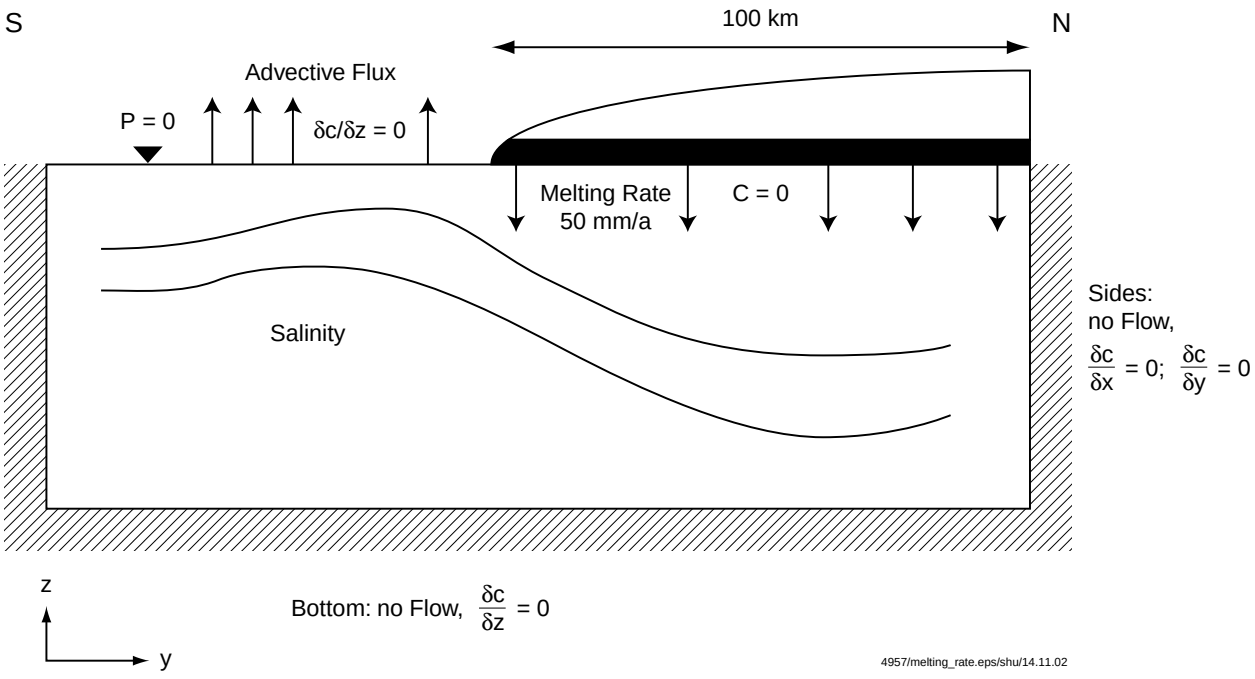

Figure 6 Boundary conditions for flow and transport.

3.9 Initial conditions

The initial salinity distribution is given as zero salinity (defined in %, by weight) from the surface down to a depth of 1000 m. Below this level, a linear increase with 10 % salinity per 1000 m is assigned up to the total depth of 4000 m. Thus, in the model the fluid density at 4000 m is about 1200 kg/m^3 and corresponds approximately to the saturation density of the fluid.

These high values of fluid density in the lower part of the model were obtained by extrapolating concentration values /Svensson, 2002a/ measured at around 1500 m in a deep borehole (KLX02: Laxemar). According to /Rhén et al, 1997/ the source for this high salinity at depth may be either an evaporite or long–term leaching of the rock; this brine seems to exist in a stagnant environment which has been isolated from meteoric influx for more than 1 million years.

Therefore, some uncertainty is associated with the fluid density prevailing below the depth of 2000 m. The assumed initial salinity distribution (at depth) deserves further investigations as its influence on the modelling results has not been assessed within the framework of this study.

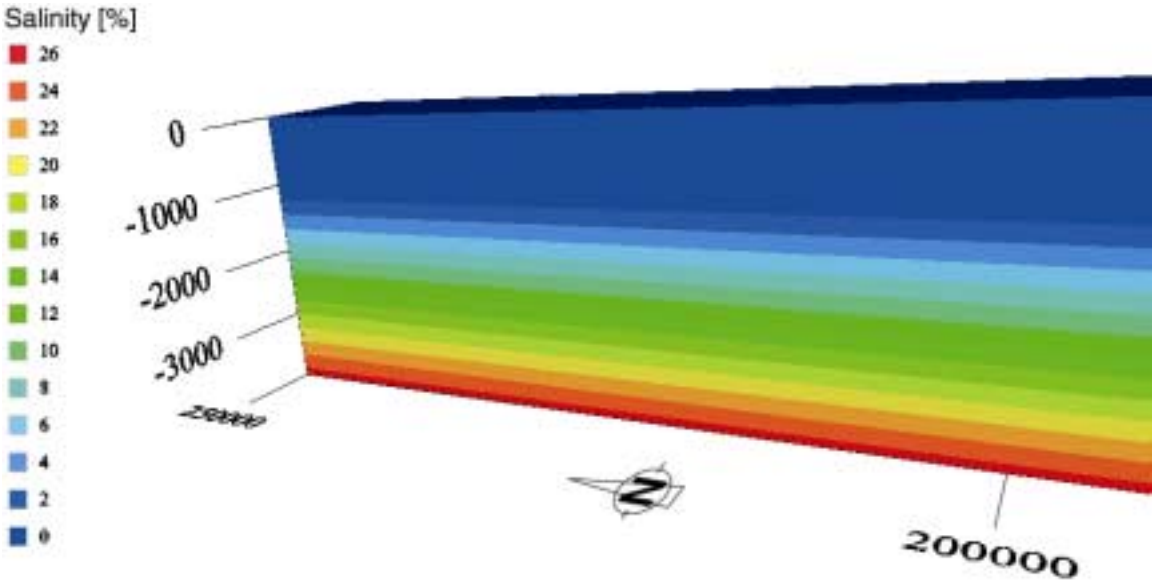

Figure 7 Initial conditions: spatial distribution of salinity.

4 Simulation

4.1 Stochastic simulation

The characterisation of the log-conductivity of the rock mass requires the generation of a realisation of the Gaussian random function model with an exponential variogram (cf section 3.5). The log-conductivity is simulated in 3 dimensions using the turning bands method /Chilès and Delfiner, 1999; Lantuéjoul, 2002/ implemented in NAMMU /Marsic et al, 2001/. The result is a Gaussian normalised simulation of the log-permeability (i.e. with zero mean and unit variance). This simulation is then scaled according to the parameters related to the hydrogeological units defined in Table 1 (cf section 3.5).

The calculation of the porosity and the integration of the major fractures zones are achieved using the approach described in section 3.5. Finally, conductivity and porosity values are assigned to each finite element of the mesh. Figure 8 illustrates the horizontal log-conductivity and porosity fields for a central segment of the model's bottom. The presence of the major fracture zones can be observed; their hydraulic influence is implicitly reproduced using the IFZ method (cf section 3.5). The corresponding statistics of the realisation are given in Table 4.

Table 4 Stochastic realisation: mean values of hydraulic properties.

Hydrogeological unit	Geometric mean of the simulated hydraulic conductivity[1)]	Arithmetic mean of the porosity	Geometric mean (input) of the hydraulic conductivity[1), 2)]
	[m/s]	[–]	[m/s]
1: ice tunnel	to be calibrated	1	–
2: 0–200	$1.7 \cdot 10^{-7}$	$9.8 \cdot 10^{-4}$	$1.3 \cdot 10^{-7}$
3: 200–400	$2.3 \cdot 10^{-7}$	$6.3 \cdot 10^{-4}$	$2.0 \cdot 10^{-7}$
4: 400–600	$2.2 \cdot 10^{-7}$	$8.1 \cdot 10^{-4}$	$2.6 \cdot 10^{-7}$
5: 600–4000	$4.8 \cdot 10^{-8}$	$2.3 \cdot 10^{-4}$	$4.7 \cdot 10^{-8}$

1) Equal to the mean of the log-conductivity values.
2) Cf Table 1.

The discrepancies between the geometric means of the realisation and their input values are related to the effect of the major fracture zones and the usual statistical fluctuations associated with a given realisation. A verification of the characteristics of the model (i.e. a Gaussian distribution with an exponential variogram) is performed. The results are shown in Figure 9. The symmetric shape of the log-conductivity histogram for the lower hydrogeological unit is of the Gaussian type. The experimental variogram calculated for a portion of the model domain can be fitted with an exponential model with a correlation scale of 275 m.

The input statistical parameters of the generated stochastic realisation (of the hydraulic conductivity) can be reproduced; ergodicity problems are thus avoided when simulating the hydraulic conductivity. Then, the effects of the spatial variability of the hydraulic properties on modelling results are assessed using a single realisation.

The end result is a 3-dimensional simulation of the hydraulic conductivity and porosity which serve as input for the numerical modelling of flow and transport processes.

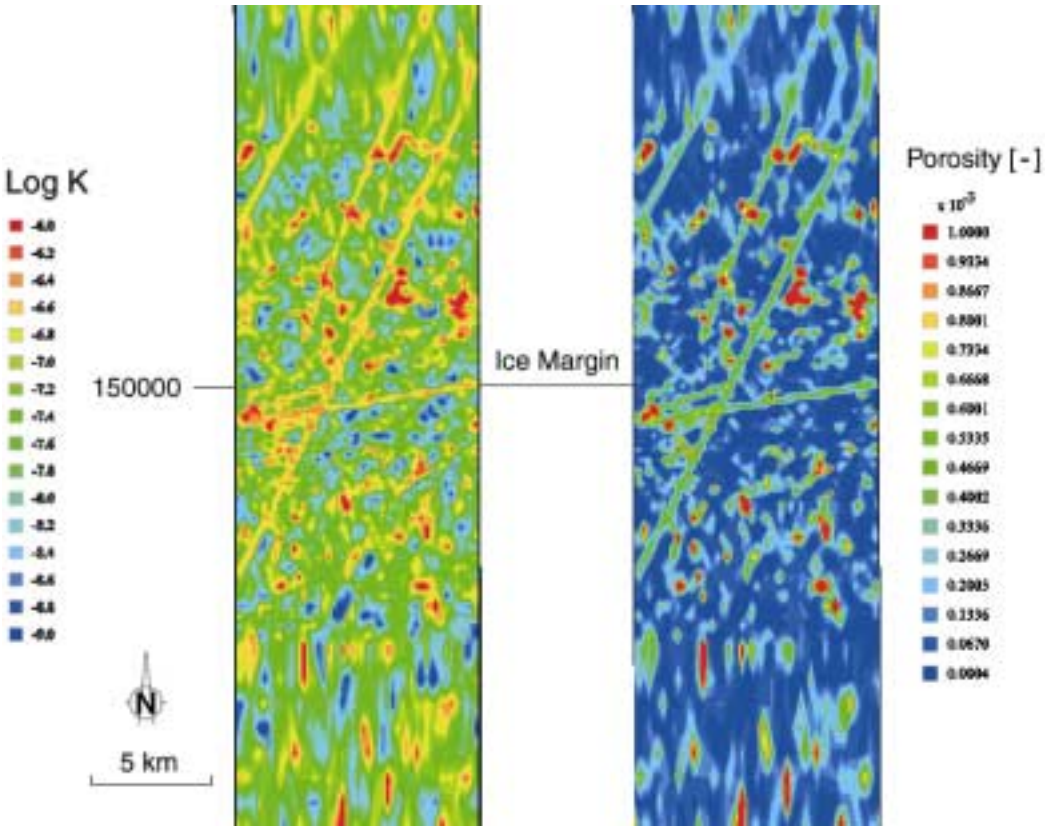

Figure 8 Stochastic simulation: log-conductivity and porosity fields (horizontal cut at a depth of 4000 m for a portion of the model domain).

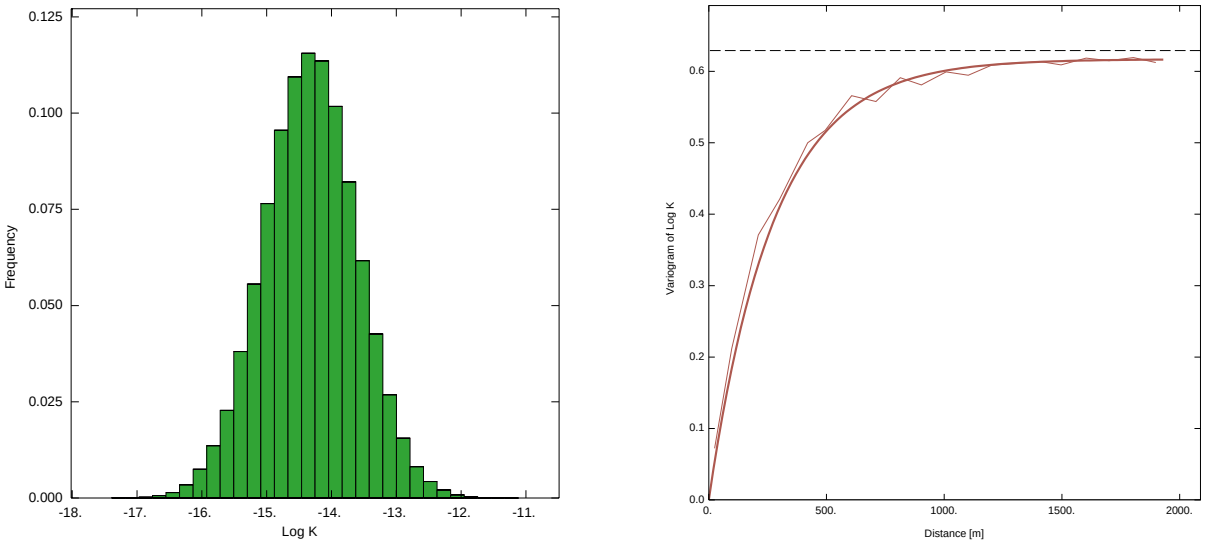

Figure 9 Log-permeability (in m^2): histogram of unit 5; experimental and exponential (bold line) variograms calculated for a portion of the model domain: 10 × 10 × 4 km^3 (horizontal dashed line at the level of the variance).

4.2 Freshwater simulation

This initial simulation, S_{calib}, performed under freshwater and steady-state conditions aims at calibrating the hydraulic conductivity of the ice tunnels. The conductivity value is considered to be constant along the ice tunnels. The flow boundary conditions match those described in section 3.8. No salt boundary conditions are needed as the initial conditions correspond to zero salinity everywhere in the model domain.

The calibration is achieved by varying the conductivity of the ice tunnels under the following criteria /Selroos, 2001/:

(1) The pressure of the water is maintained under the ice load such that the ice does not lift:

$$p - p_{ice} < 0 \qquad (11)$$

$$p_{ice} = 920 \cdot 9.81 \cdot \sqrt{11.08 \cdot l}$$

where:

p_{ice} = ice load, expressed in terms of pressure

l = distance from the ice margin

(2) The gradient in the ice tunnels should be approximately 15 m/km.

The pressure of the water can be allowed to exceed the ice load close to the margin, where the glacier in reality functions as a leaking confining system and artesian waters are released on the ice surface.

Several simulations were performed for various hydraulic conductivity values of the ice tunnels (see Figures 10 and 11). The difference between the pressure of the water and the ice load (equation (11)) is calculated for each node along the surface of the model (i.e. below the ice).

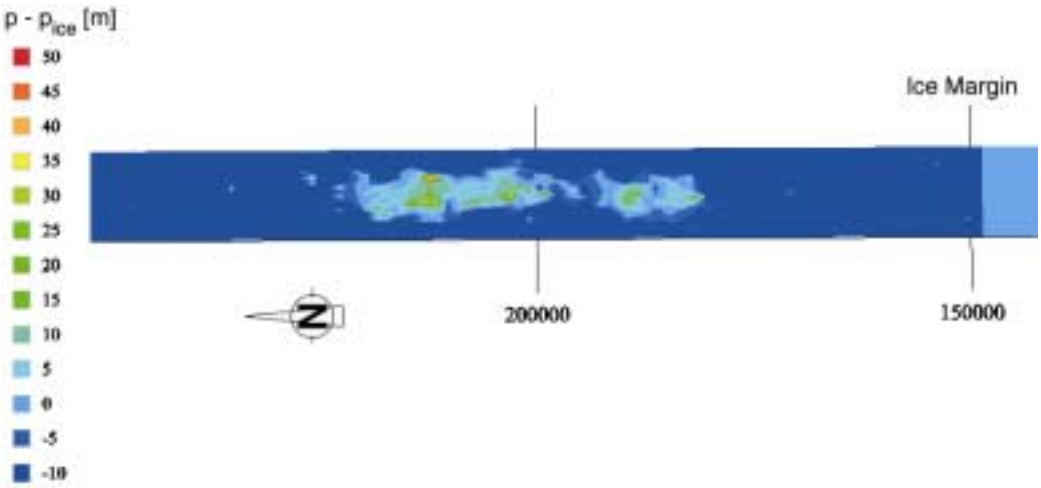

Figure 10 Freshwater simulation with $K_{ice\ tunnel}$ = 1 m/s: occurrence of zones where the pressure of the water exceeds the ice load.

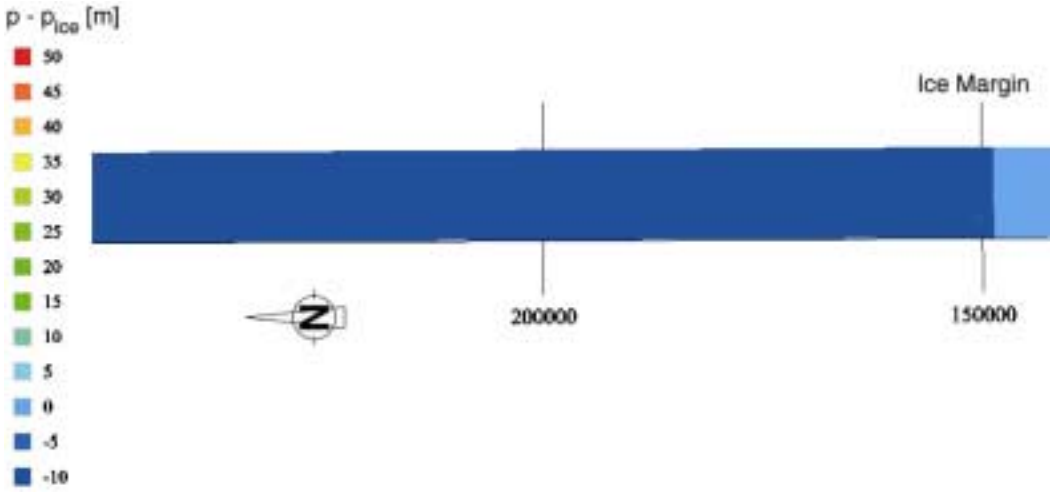

Figure 11 Calibrated freshwater simulation, S_{calib}, with $K_{ice\ tunnel}$ = 2 m/s.

For a hydraulic conductivity value of 2 m/s for the ice tunnels, the calibration criteria can be considered to be met. Three nodes still present a positive pressure difference, but these nodes are associated with very low conductivity values (due to the stochastic variability of the conductivity field); eliminating them by increasing the ice tunnel conductivity would lead to an unrealistic flow field. Therefore, it was decided to keep the effect (occurring at small scale) of these nodes. The corresponding (maximum) value of the gradient within the ice tunnels obtained is equal to 7 m/km, which is close to the target value foreseen. The calibrated value of the hydraulic conductivity, when translated in terms of transmissivity is comparable (up to a factor of 2) to the one obtained by /Svensson, 1999/.

The calibrated hydraulic head field of the freshwater simulation, S_{calib}, is shown in Figure 12. The irregular shapes observed for the head iso-surfaces are a consequence of the spatial variability of the rock mass hydraulic conductivity (cf section 4.1).

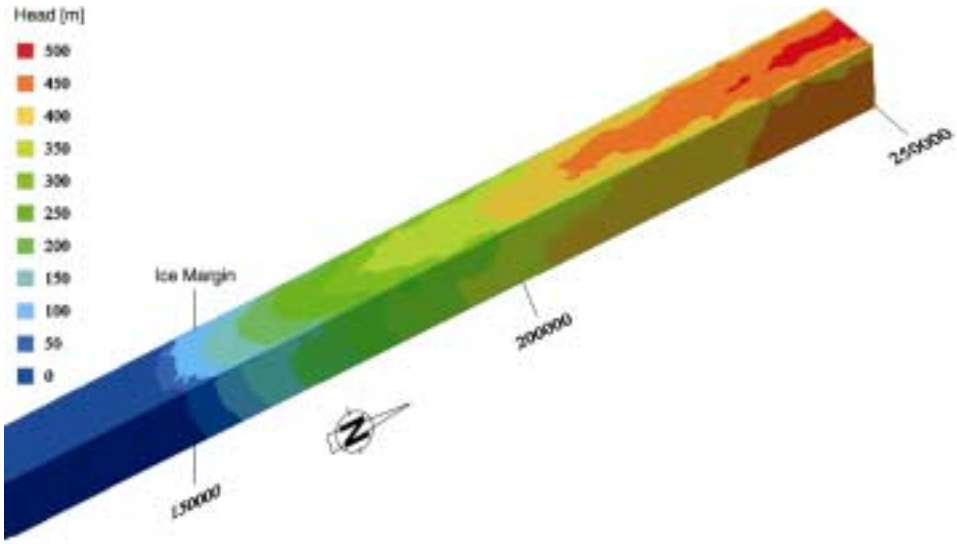

Figure 12 Calibrated freshwater simulation, S_{calib}: hydraulic head field.

4.3 Salt simulation

The base case simulation, S0, of coupled flow and salt transport is performed using the parameters and the boundary/initial conditions defined above (cf sections 3.5, 3.6, 3.8 and 3.9). Although all the boundary conditions are steady state conditions, the problem to be solved is transient due to the freshwater input of the glacier that perturbs the initially stratified salinity distribution. This freshwater contribution causes variations in density, with the result that groundwater flow becomes transient. This coupling of groundwater flow and salt transport requires the resolution of a set of non-linear equations (cf section 3.4) in order to simulate the flow field evolution due to the mixing of water with variable salinity.

4.3.1 Numerical choices

The set of non-linear equations is solved with a Newton-Raphson iteration scheme. The GMRES iterative solver of NAMMU /Marsic et al, 2001/ is used to solve the equations in each Newton-Raphson iteration. GMRES (Generalized Minimal Residual) is a Krylov-based iterative method for the solution of linear systems associated to unsymmetric matrices. For the time discretisation, a fully implicit Crank-Nicholson transient scheme is used. The numerical parameters selected for the simulation are listed in Table 5.

Table 5 Numerical parameters.

GMRES convergence criterion	Newton-Raphson convergence criteria	Time stepping
10^{-5}	10^{-3}	automatic selection

4.3.2 Results

Simulation S0 is run for a model duration of about 150 years. The motivation for this shorter duration compared to the 1000 year period chosen by /Svensson, 1999/ is found in the close resemblance of the results even after short simulation periods (cf section 4.3.3).

Within the framework of this study, the spatially variable hydraulic conductivity of the rock mass has been considered as a scalar (cf section 3.5) at the scale of the mesh element. Attempts to take into account a tensor for the rock mass conductivity have led to unacceptable run times. With the increase in heterogeneity introduced by the tensor, run times are prolonged because of the augmented number of iterations required to solve the non-linear problem. Consequently, this option was abandoned.

The calibrated hydraulic conductivity value of the ice tunnels (K = 2 m/s) is also applicable for the base case simulation S0. A test performed after 32 years of simulation has shown that the calibration criteria were met (cf section 4.2). The ice tunnels are located at the surface under the glacier and are in direct contact with the melting zone. Mainly freshwater circulates within the ice tunnels; as a consequence, the calibrated conductivity value remains valid.

A comparison of the equivalent freshwater head field from simulation S0 (Figure 13) with the hydraulic head field from the calibrated simulation, S_{calib} (Figure 12) makes apparent the significance of density effects in groundwater flow.

The distribution of the Darcy velocity vectors for the time of 100 years is presented in Figures 14 and 15. In the horizontal cut, one can observe the relevance of the ice tunnels with respect to subglacial groundwater flow; the main fraction of the meltwater is discharged through the ice tunnels. The decrease of the Darcy velocity with depth is demonstrated in the vertical cut.

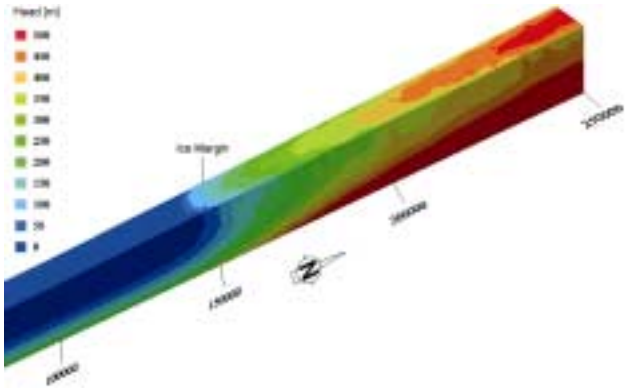

Figure 13 Simulation S0: equivalent freshwater head at 100 years.

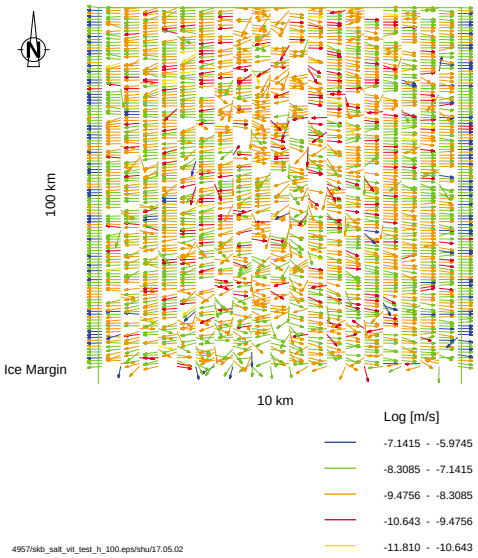

Figure 14 Horizontal cut: Darcy velocity vectors at ground level at 100 years.

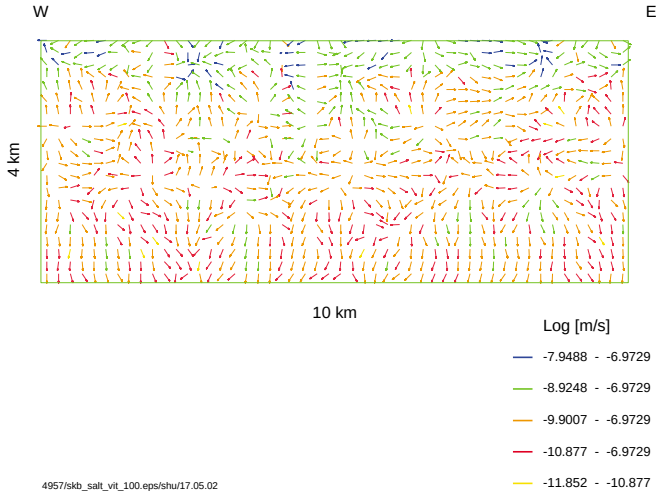

Figure 15 Vertical cut (1 km North of the ice margin): Darcy velocity vectors at 100 years.

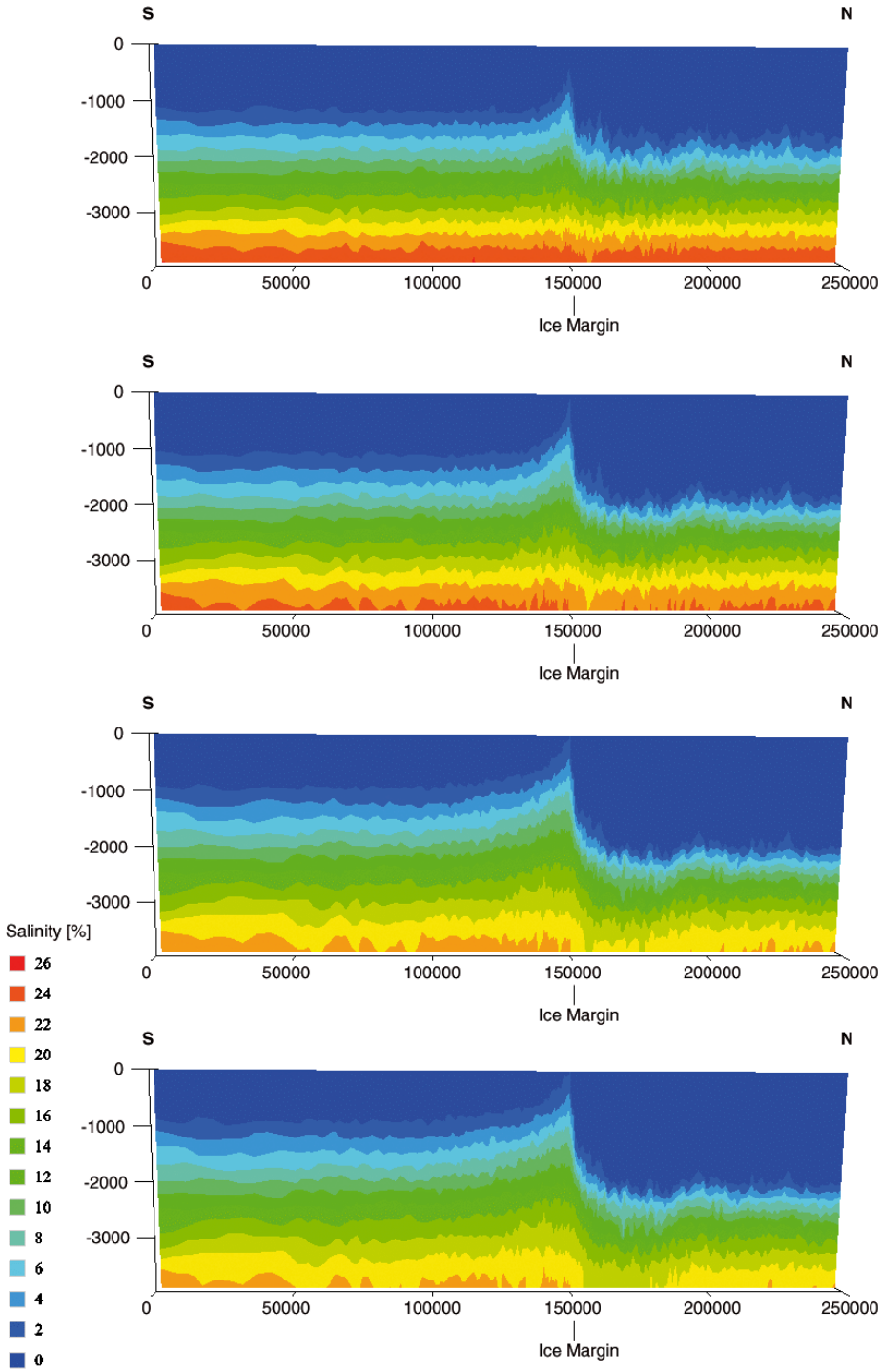

Figure 16 Cross-section A-A: salinity at times 13, 32, 100 and 122 years (from top to bottom).

This effect is related to the decrease in permeability (cf Table 1; section 3.5) as well as to the increase in salinity with depth.

Vertical cross-sections (with orientations matching those of cross-sections A-A and B-B in Figure 1, cf section 3.1) of the salinity were generated for the following times: 13, 32, 100 and 122 years (see Figures 16 and 17). The transient effect of the glacier in the Northern part of the model has the following consequences: (a) North of the ice margin, the salinity

front is pushed downward due to the freshwater input of the glacier; after 122 years, the salinity front has shifted from a depth of –1000 m to about –2000 m; (b) due to the groundwater flow induced by the freshwater input, the Southern part of the model sees the salinity front moving slightly upwards; (c) because of their high salinity, the high density zones located at depth South of the ice margin, tend to move towards the North of the ice margin where less dense zones occur and (d) fingering effects due to the spatially variable hydraulic conductivity are observed (cf Figure 16). These last two density effects enhance mixing and salt transfer processes.

The Svensson simulation results (cf Figure 1) in a deeper penetration depth of the salt water interface when compared to the current results (cf Figure 16). This outcome is related to a different distribution of the water infiltrating from the melting zone /Svensson, 1999/.

The potential for reaching steady-state conditions is investigated by tracing the evolution of the salt mass in the model (see Figure 18). The salt mass does not appear to stabilise within the time period considered. It is believed that quasi steady-state conditions can not be reached in the near future (within several hundred if not several thousand years). Due to the chosen salt boundary conditions (cf section 3.8), salt will continue to be removed with time until most of the model domain becomes completely deprived of salt.

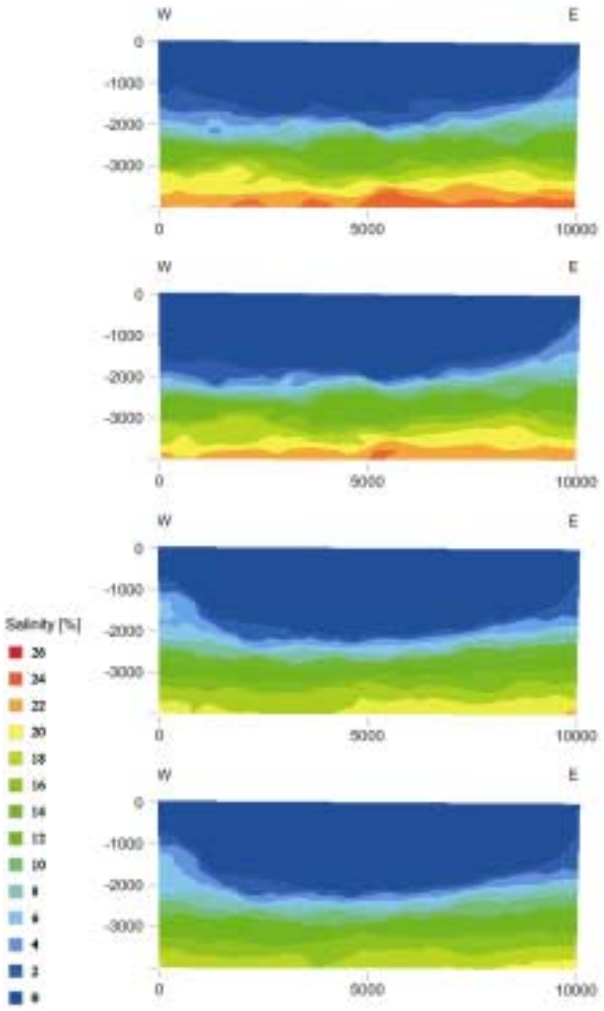

Figure 17 Cross-section B-B (located 25 km North of the ice margin): salinity at times 13, 32, 100 and 122 years (from top to bottom).

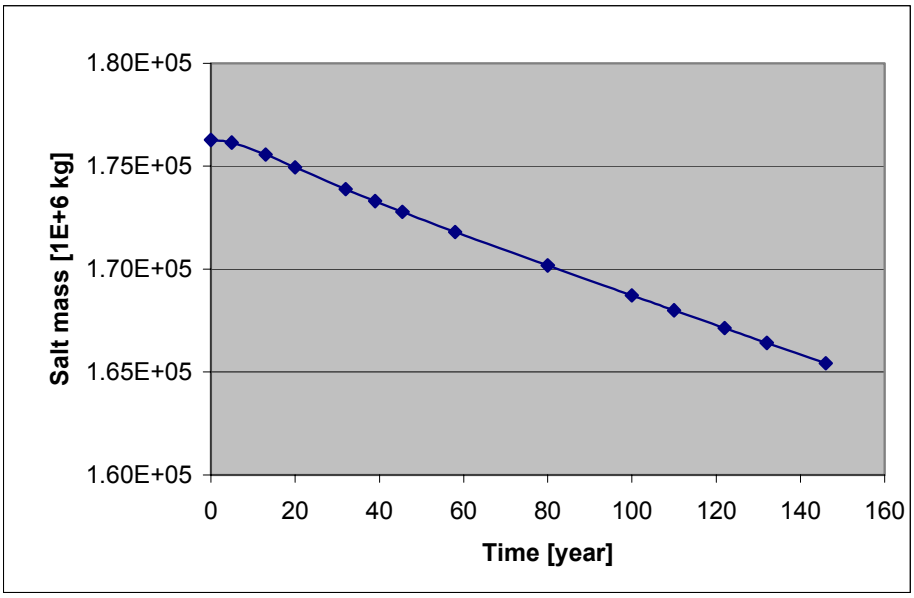

Figure 18 Evolution of the salt mass in the model.

4.3.3 Comparison with /Svensson, 1999/

As mentioned above, the time scale at which salt transfer occurs in the current model is almost ten times smaller than the one obtained by /Svensson, 1999/. The differences between the modelling approaches are summarised in Table 6. It appears that the values of the parameters porosity, infiltration, correlation scale and dispersivity differ significantly compared to the ones used by /Svensson, 1999/. The values of all these parameters in the current model tend to favour salt transfer within the model domain. However, the porosity is the key parameter to explain the differences in time scales. Its dominant role has been assessed by performing simplified calculations in two dimensions (see Appendix A).

Table 6 Differences between modelling approaches.

Parameters/ boundary conditions	/Svensson, 1999/	Current choices	Influence on flow	Influence on transport
Width of ice tunnel	200 m	5 m	+	+
Correlation scale	0	275 m	++	++
Porosity	**0.001**	**mean(600–4000m) = $2.3 \cdot 10^{-4}$** (cf Table 4)	**+**	**+++**
Infiltration zone	125–225 km	150–250 km	++	++
Infiltration	variable with a maximum value of 50 mm/a	50 mm/a	++	++
Molecular diffusion	none	$3 \cdot 10^{-9}$ m^2/s	–	+
Dispersivity	$\alpha_T = \alpha_L = 5\,m$	$\alpha_T = 50\,; \alpha_L = 100\,m$	–	++

4.3.4 Numerical difficulties

Beyond 150 years of salt simulation, anomalous values of concentration start to appear at the surface of the model close to the ice margin. At this location, no dispersive flux boundary conditions apply (cf section 3.8). With such boundary condition for advection-dominated cases, the error introduced by restricting the mass flux across the boundary to its advective contribution is negligible. But the simulated case, S0, is diffusion dominated near the ice margin which causes a biased concentration profile near the boundary. This numerical problem could be solved by applying a free-exit boundary condition along the surface of the model, South of the ice margin. Such a boundary condition can be expressed as follows /Cirpka, 1999/:

$$\mathbf{n} \cdot \nabla \cdot (\rho \mathbf{q} c - \phi \rho \mathbf{D} \cdot \nabla c) = 0 \qquad (12)$$

An additional complication is posed by the large run-times associated with the simulations. For the selected time period and considering a fully coupled simulation, run-times could exceed a month of CPU time. One way of decreasing these times is to perform the computation in parallel mode.

4.4 Particle tracking

As no steady-state conditions can be attained when simulating salt transfer, transient particle tracking should be performed. Due to the high demands on computing time required for salt simulation (more than a month), this option is not feasible. Therefore, two discrete points in time are chosen for comparison purposes in order to select a time reference for particle tracking calculations.

4.4.1 Selection of a time reference

Two discrete points in time of the salt simulation S0 are selected for particle tracking: t1 at 100 years and t2 at 122 years. 500 particles are released along a line at the surface (i.e. at a depth of 5 m beneath the glacier). The 100 km long line follows the model's longitudinal center, beginning at the ice margin and extending North. The starting locations of the particles are spaced at equal distances along the line.

For each point in time, t1 and t2, travel times and penetration depths of the particles are recorded and displayed on histograms (see Figure 19). Similar statistical parameter values and distribution shapes are obtained for both t1 and t2. Then, t1 is selected as time reference; all the subsequent particle tracking calculations are performed using the salt simulation S0 at 100 years.

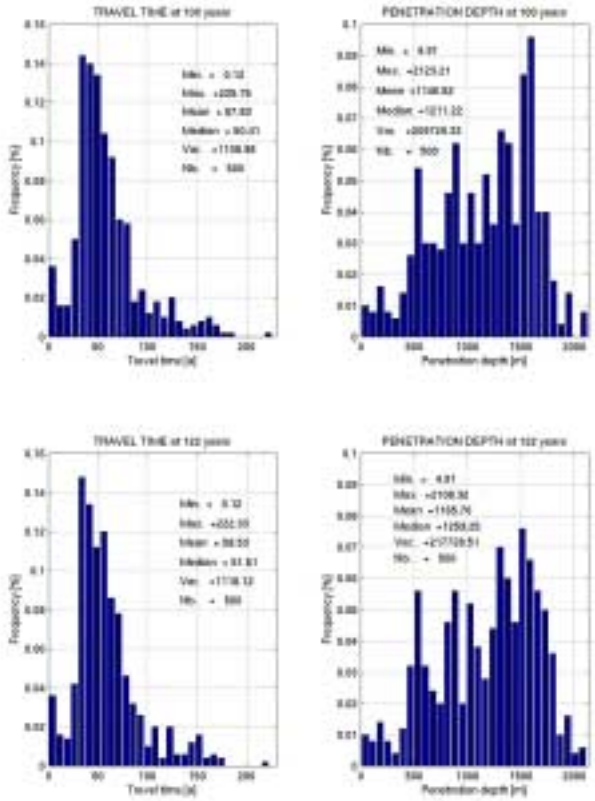

Figure 19 Histograms: travel time and penetration depth of particles at times t1 and t2 (top and bottom graphs, respectively).

4.4.2 Case P1

Case P1 aims at studying the characteristics of subglacial groundwater flow due to the basal melting of the glacier. The flow paths of basal meltwater are simulated by performing particle tracking calculations for simulation S0 at 100 years.

Again, 500 particles are released along a line at the surface (i.e. at a depth of 5 m beneath the glacier). The 100 km long line follows the model's longitudinal center, beginning at the ice margin and extending North. The y-co-ordinates of the starting locations of the particles are equally spaced; the x-co-ordinates present a random variation within a bandwidth of 100 m in order to avoid potential effects linked to regular patterns of particle starting points.

The visualisation of the particle trajectories is presented in Figures 20 and 21. The vertical cross-section illustrates the penetration depth of the particle trajectories in relation to the salinity of the water; the particle trajectories stay above the high salinity zones of the model domain and are, therefore, restricted to roughly the top 2000 m. The results show that the penetration depth of the particles is blocked by the high density of water encountered at depth (cf Figure 20). These physical outcomes are in accordance with the modelling tests performed by /Younes, 1998/.

The horizontal cut shows the importance of the drainage effect due to the ice tunnels. The distribution of the particle trajectories is asymmetric with respect to the central starting line. In the Northern part this effect is related to the spatially variable hydraulic conductivity of the rock mass; in the South, the effect is accentuated by the presence of the major fracture zones (cf Figure 4, section 3.3).

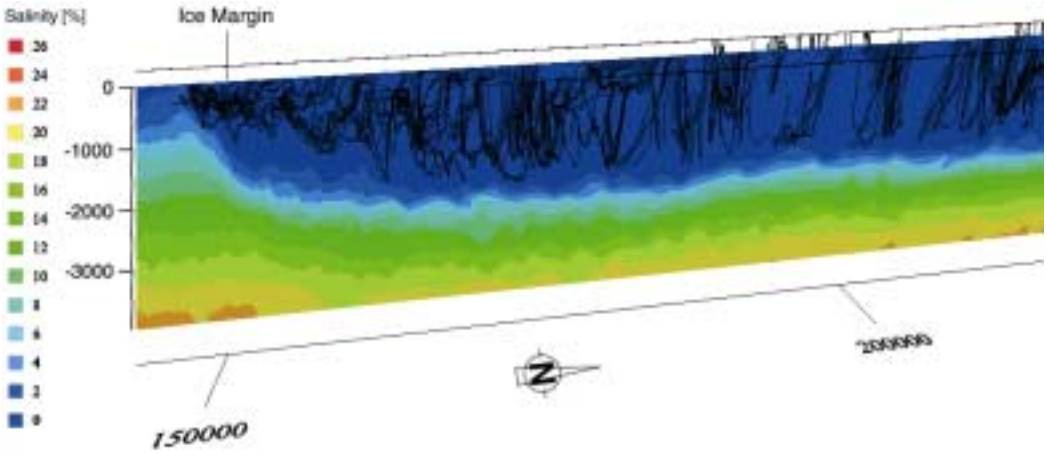

Figure 20 Case P1: vertical cross-section A-A with projected particles trajectories.

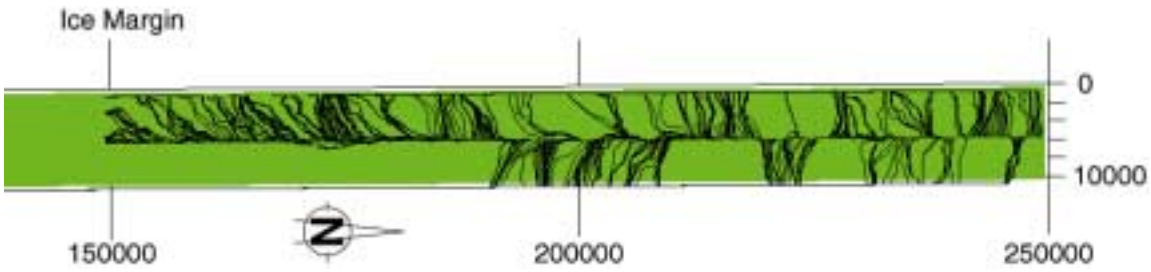

Figure 21 Case P1: horizontal cut with projected particles trajectories.

Graphs of travel time and penetration depth as a function of the distance to the ice margin are produced (see Figures 22 and 23). The maximum values for travel time occur at a distance of 25 to 75 km from the ice margin. The low values of travel time are caused by particles which are not captured by the ice tunnels; their exfiltration zones are located in front of the ice margin (cf Figure 21). Beyond about 15 km from the ice margin, penetration depths greater than 1500 m are observed.

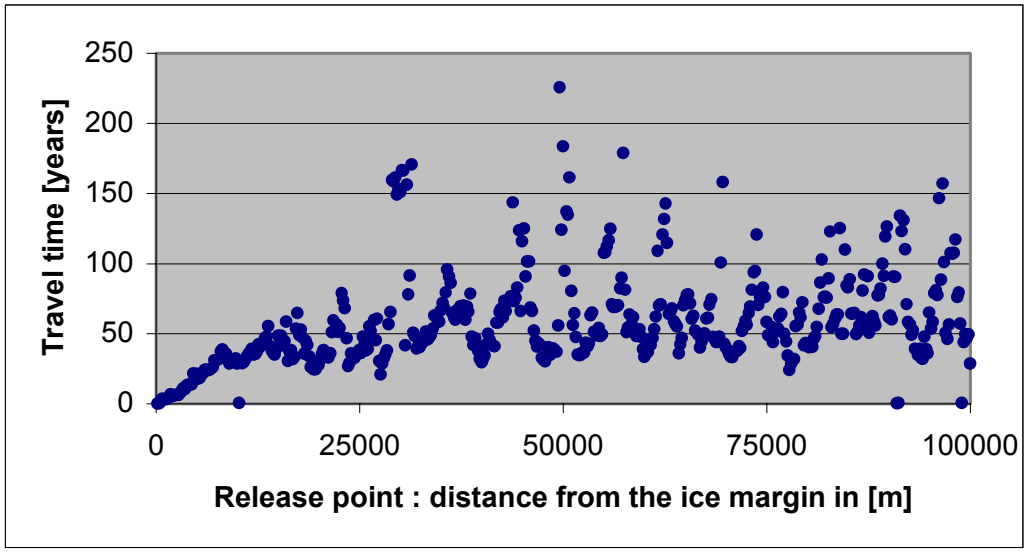

Figure 22 Case P1: travel time in relation to the location of the ice margin.

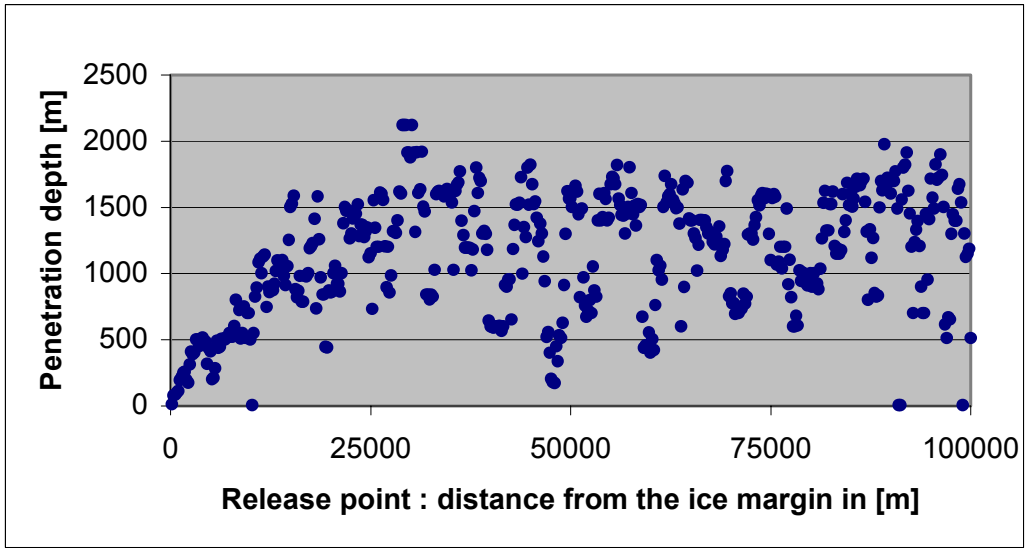

Figure 23 Case P1: penetration depth in relation to the location of the ice margin.

A major difference appears with respect to the maximum penetration depth of particles, when comparing these results with the ones of /Svensson, 1999/. In the present study, the penetration depth of particles cannot exceed 2500 metres; penetration depths below 3500 m were reached by particles in Svensson simulation. According to /Svensson, 2002a/, the shape of the infiltration as well as some numerical problems could explain this large penetration depth for some particles.

The travel time distribution to depths of 100, 250, 500 and 1000 m are recorded and visualised by means of histograms (see Figure 24). As expected, travel times are increasing with depth; a value of 26 years is obtained for the median travel time at the depth of 1000 m. This depth is reached by 64% of the particles.

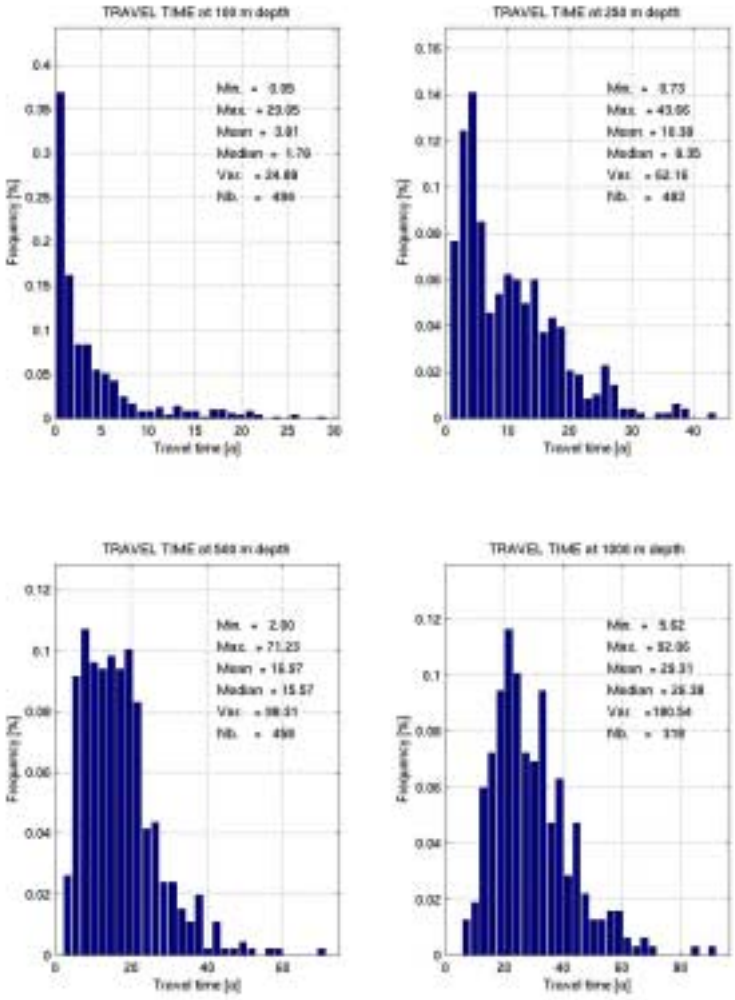

Figure 24 Case P1: histograms of travel time at depths of 100, 250, 500 and 1000 m.

4.4.3 Case P2

In order to study different conditions during a glaciation period, the repository is placed at several locations close to the Western boundary of the model and aligned along a N-S direction.

Transport from 10 repository locations at a depth of 500 m is studied by particle tracking. These locations, with an area equal to 1×1 km^2, are positioned every 10 km towards the North. 50 particle starting points are randomly distributed within each location for particle tracking computation using simulation S0 at 100 years. The travel time distribution for the 10 repository locations are recorded and visualised by means of histograms (see Figure 25).

The resulting travel times present median values in the range from 1 to 8 years. These short travel times result from the proximity of the repository locations to the ice tunnel with a strong drainage effect.

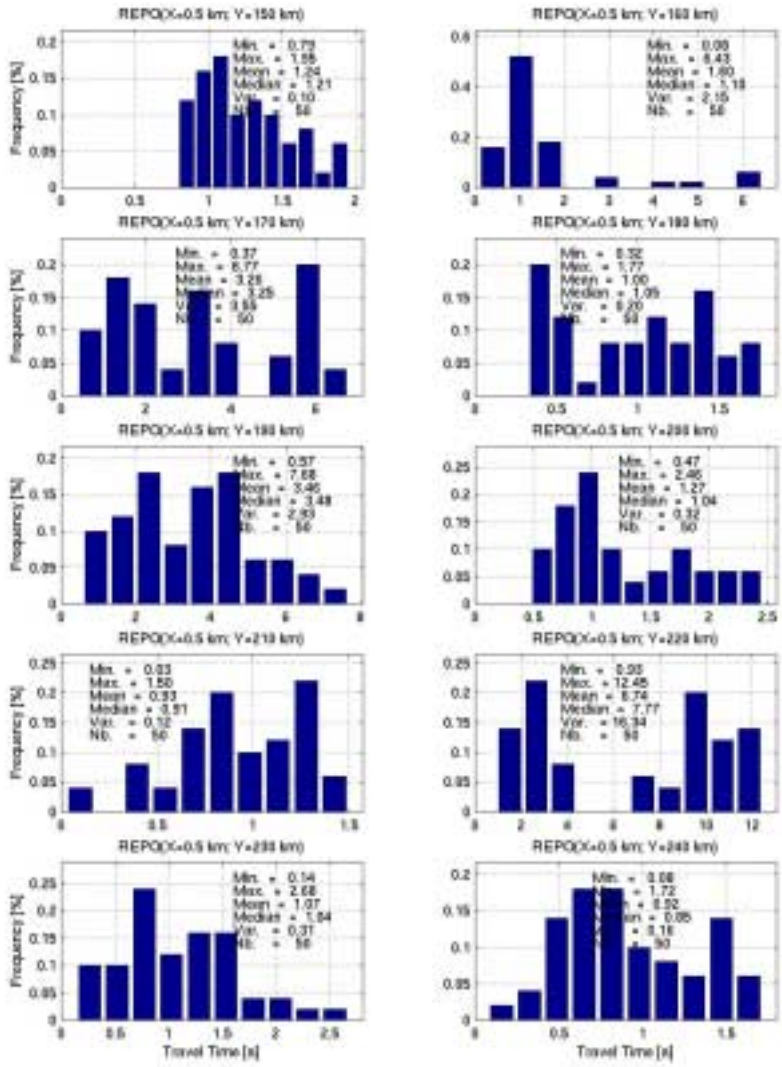

Figure 25 Case P2: histograms of travel time for 10 repository locations (West side of the domain).

The Darcy velocity at particle starting positions for each repository locations are displayed on Figure 26. Except for the repository location at the ice margin, the variability of the velocity is rather similar when locations are compared.

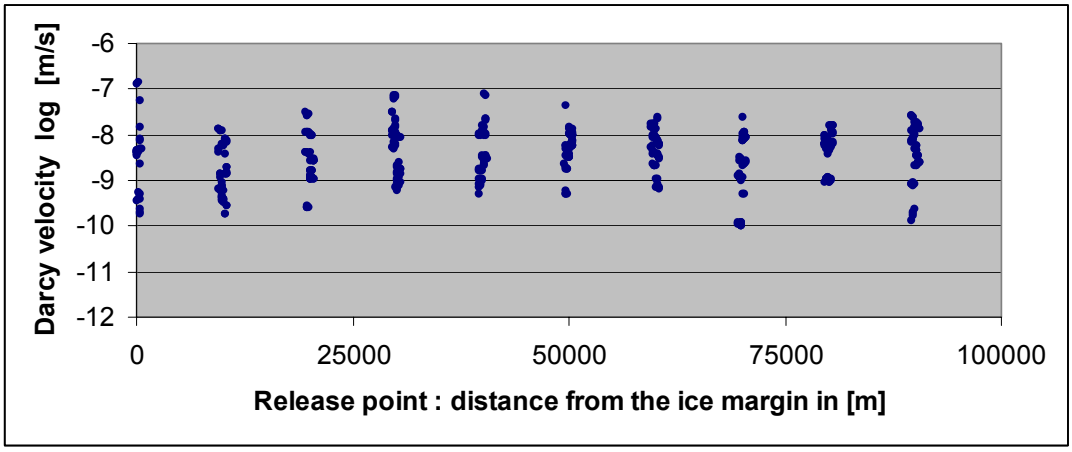

Figure 26 Case P2: Darcy velocity at particle starting positions.

4.4.4 Case P3

Case P3 is identical to case P2, with the difference that the 10 repository locations are now positioned in the middle of the model domain (i.e. at mid-distance between the ice tunnels). As before, 50 particle starting points are randomly distributed within each repository location. The travel time distribution for the 10 repository locations are recorded and visualised by means of histograms (see Figure 27).

The obtained travel times present median values in the range from 1 to 126 years**.** The lowest median value stems from a repository location situated under the ice margin. The fast travel times associated with it are caused by particles that exfiltrate in front of the ice margin. At this location, the boundary condition (p = 0, South of the ice margin; cf section 3.8), above the repository, steer groundwater flow towards the surface.

The Darcy velocity at particle starting positions for each repository locations are displayed on Figure 28. Except for the high values observed at the repository location close to the ice margin, the variability of the velocity is rather similar when locations are compared.

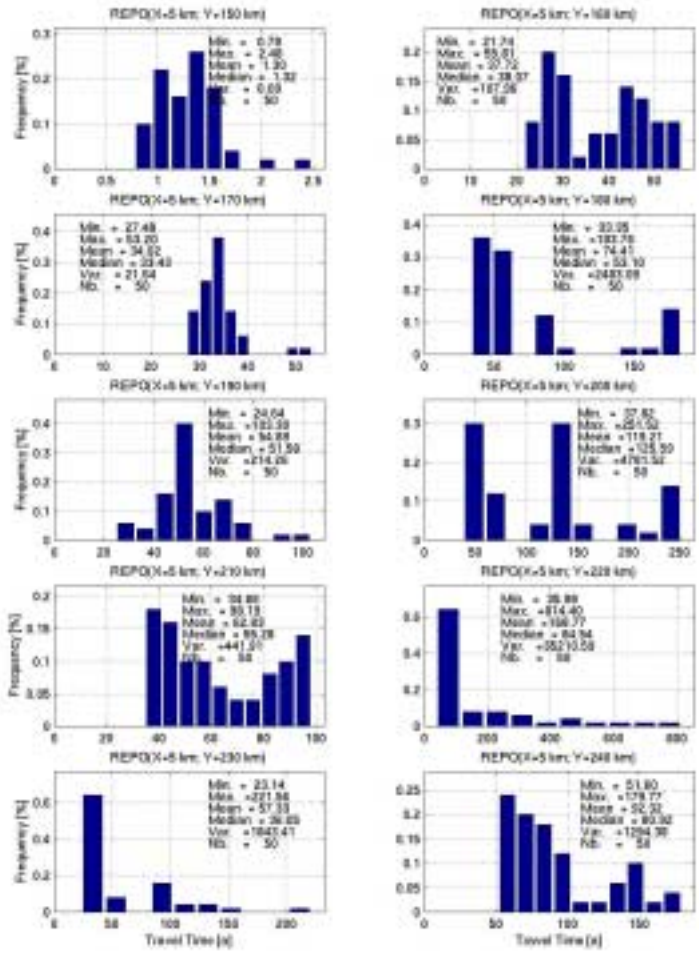

Figure 27 Case P3: histograms of travel time for 10 repository locations (middle of the domain).

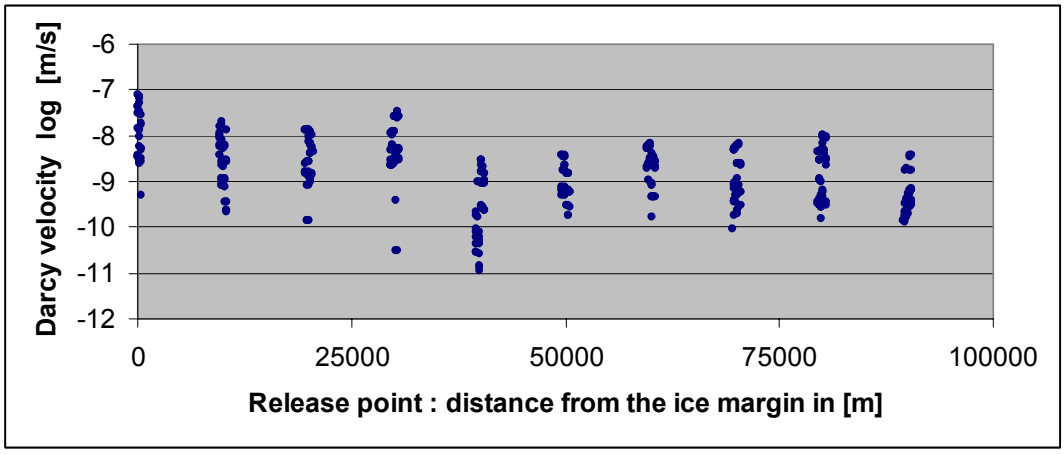

Figure 28 Case P3: Darcy velocity at particle starting positions.

5 Conclusions and recommendations

The objectives proposed for the groundwater flow and transport modelling for period of glaciation have been met:

- The results have shown the importance of the ice tunnels in governing subglacial groundwater flow due to basal ice melting. The influence of the ice tunnels on the salinity distribution is significant as is their impact on the flow trajectories and, hence, on the resulting travel times.
- The results of simulation S0 have revealed that no steady-state flow conditions are reached. Due to the chosen salt boundary conditions, salt will continue to be removed with time until most of the model domain becomes completely deprived of salt within a few thousand years. Because the brines at depth appear to be in a stagnant environment and are potentially more than 1 million years of age, the assumed hydraulic conductivity for the depth interval of –2000 to –4000 m is probably too high; as a result, this water at depth is flushed out too fast in the model.
- The impact of subglacial groundwater flow has been assessed on a repository with respect to its position to the ice margin. Travel times increase by about one order of magnitude for repository locations distant from the ice tunnels (positioned at mid-distance between the ice tunnels). Such repository locations, when situated close to the ice margin associate with them a decrease in the travel times by a factor of 30.
- Some parameters and boundary conditions of the current model differ from the previous study of /Svensson, 1999/ as newly available information has been integrated. Their impacts on the modelling results have been evaluated. The porosity used in the current model has proven most influential in reducing the time scale at which salt transfer occurs. The reduction was almost by a factor of 10 as compared to the previous study.
- The NAMMU package (version 7.1.1) has allowed for large 3D simulations of density-driven flow (fully coupled) induced by variable salinity of the groundwater. Several tests were performed and the obtained results were conclusive. NAMMU is now completely integrated into Colenco's computing environment to have a series of pre- and post-processing tools readily available (cf Appendix B). (NAMMU has rather limited pre- and post-processing capabilities.)
- This integration allows to dispose of the required pre- and post-processing capabilities which are rather limited in NAMMU.

Improvements in the treatment of salt boundary conditions in NAMMU are needed. A free-exit type of boundary condition should be introduced in order to avoid potential numerical difficulties.

In order to solve systems with a large number of unknowns (more than a million), an additional numerical method may be introduced into NAMMU whereby the resolution of the flow and transport equations is performed sequentially within the same non-linear iteration. In other terms, this technique could handle larger systems than NAMMU method with the same amount of RAM.

The following recommendations regarding additional work and open issues can be formulated:

- Sensitivity studies using the current model under freshwater conditions. The main parameters to be analysed are: (a) the rock mass hydraulic conductivity at depth, (b) the spatially variable hydraulic conductivity for the ice tunnels with a behaviour corresponding to the evolution of the transmissivity in a river, (c) the rock mass hydraulic conductivity as a tensor, and (d) the melting rate.
- Sensitivity studies with the current salt model. The main parameters to be analysed are: (a) the correlation between hydraulic conductivity and porosity, and (b) the dispersivity. In terms of initial conditions, the occurrence of sea water South of the ice margin should be examined. Its impact on the salt simulation results could then be assessed by comparison with the base case S0.
- Development of an upscaling procedure using stochastic simulations for finite-element meshes with cuboid elements of irregular size.

The modelling approach applied for the study of glaciation effects at Äspö has successfully described the assumed conditions and relevant processes. It may certainly serve as a well founded base for future modelling tasks to provide solutions to further questions.

6 References

Boulton G S, Zatsepin S, Maillot B, 2001. Analysis of groundwater flow beneath ice sheets, SKB TR-01-06, Svensk Kärnbränslehantering AB.

Chilès J P, Delfiner P, 1999. Geostatistics: modelling spatial uncertainty, Wiley Series in Probability and Mathematical Statistics, 695p.

Cirpka O A, 1999. Numerical methods for groundwater flow and transport, Class CEE362 "Advanced Topics in Subsurface Transport", Stanford University, 148p. http://www.iws.uni-stuttgart.de/~cirpka/CEE362notes.pdf

Cliffe K A, Morris S T, Porter J D, 1998. Assessment model validity document, NAMMU: a program for calculating groundwater flow and transport through porous media, SKB R-99-51, Svensk Kärnbränslehantering AB.

Lantuéjoul C, 2002. Geostatistical simulation: models and algorithms, Springer, 256p.

Marsic N, Hartley L, Jackson P, Poole M, Morvik A, 2001. Development of hydrogeological modelling tools based on NAMMU, SKB R-01-49, Svensk Kärnbränslehantering AB.

Rhén I, Gustafson G, Stanfors R, Wikberg P, 1997. Äspö HRL – Geoscientific evaluation 1997/5. Models based on site characterisation 1986–1995. SKB TR-97-06, Svensk Kärnbränslehantering AB.

Selroos J O, 2001. Glaciation meeting at SKB on June 19, 2001.

Siegel P, Mosé P, Ackerer P, Jaffré J, 1997. Solution of the advection dispersion equation using a combination of discontinuous and mixed finite elements, Int. J. for Numerical Methods in Fluids, 24, pp.595–613.

SR 97, 1999. Post-Closure safety, SKB TR-99-06, Volume II, Svensk Kärnbränslehantering AB.

Svensson U, 2002a. Personal communication.

Svensson U, 2002b. Official communication at SKB meeting on March 6, 2002.

Svensson U, 1999. Subglacial groundwater flow at Äspö as governed by basal melting and ice tunnels, SKB R-99-38, Svensk Kärnbränslehantering AB.

Vidstrand P, 2001. BENCHPAR, Progress Report October 2000 – February 2001, CTH.

Younes A, 1998. Modélisation de l'écoulement et du transport de masse en milieu poreux avec les éléments finis mixtes et discontinus – prise en compte du contraste de masse volumique et de viscosité, Laboratoire d'Hydrodynamique des Milieux Poreux, Thèse, Université Louis Pasteur, Strasbourg, France, 181p.

Appendix A

Influence of the porosity

Objective

In order to evaluate the influence of the porosity on the 3D modelling results, flow and transport simulations are performed in 2 dimensions using the mixed finite element method (program MHYTIC: /Siegel et al, 1997/).

Geometry

The modelled domain corresponds to the 2D vertical cut B-B with an E-W orientation and a location 25 km North of the ice margin. The vertical variations for the hydraulic conductivity are considered in deterministic manner (see Figure A1).

Modelling approach

The flow conditions are steady state with an infiltration at the top (50 mm/year). At the ice tunnel locations, a prescribed head (H=0 m) is imposed. The initial concentration in salt is the same as for the 3D model (cf section 3.9). There is no coupling term between flow and transport; the density does not play any role in the calculations. The absence of coupling effects is likely to increase the evolution rate of the salt transfer processes. However, the assessment of the influence of the porosity can be performed by sensitivity calculations.

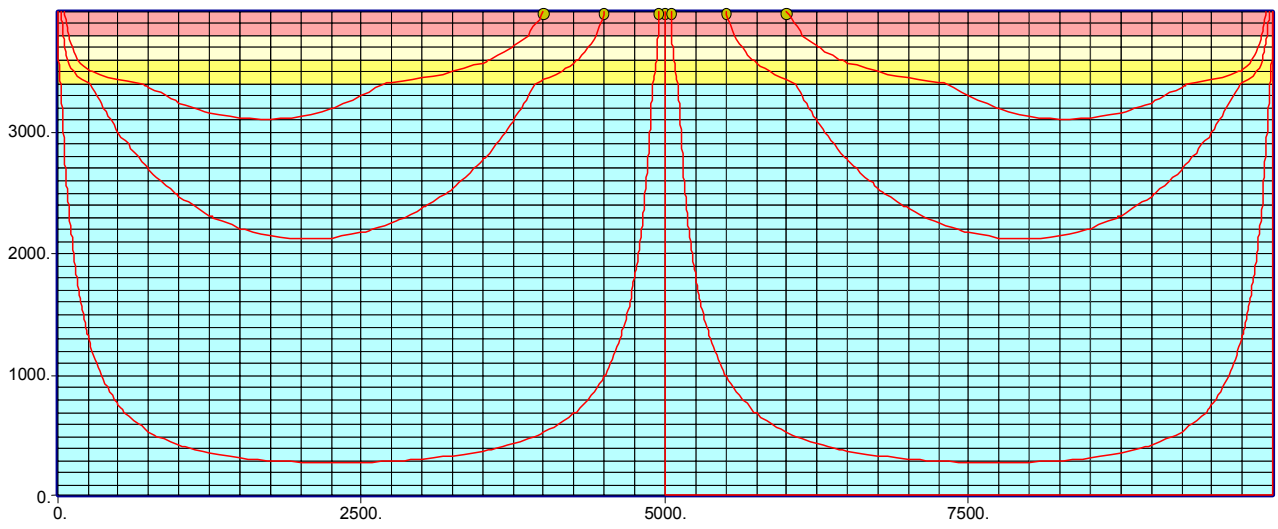

Figure A1 Cut B-B: finite-element mesh, hydrogeological units and particle trajectories.

Simulations

Case 1 (see Table A1) uses a constant porosity value equal to 0.001 like in the study of /Svensson, 1999/. Case 2 applies constant values of porosity for each hydrogeologic unit (see Table A2). These values correspond to the arithmetic mean of the porosity estimated from the NAMMU stochastic realisation. The simulated hydraulic head for cases 1 and 2 is given in Figure A2.

Table A1 Case 1: hydraulic parameters.

Hydrogeological unit	Hydraulic conductivity[1)] [m/s]	Porosity [–]
2: 0–200	$1.3 \cdot 10^{-7}$	0.001
3: 200–400	$2.0 \cdot 10^{-7}$	0.001
4: 400–600	$2.6 \cdot 10^{-7}$	0.001
5: 600–4000	$4.7 \cdot 10^{-8}$	0.001

1) Cf section 3.5.

Table A2 Case 2: hydraulic parameters.

Hydrogeological unit	Hydraulic conductivity[2)] [m/s]	Arithmetic mean of the porosity[3)] [–]
2: 0–200	$1.3 \cdot 10^{-7}$	$9.8 \cdot 10^{-4}$
3: 200–400	$2.0 \cdot 10^{-7}$	$6.3 \cdot 10^{-4}$
4: 400–600	$2.6 \cdot 10^{-7}$	$8.1 \cdot 10^{-4}$
5: 600–4000	$4.7 \cdot 10^{-8}$	$2.3 \cdot 10^{-4}$

2) Cf section 3.5.
3) Cf section 4.1

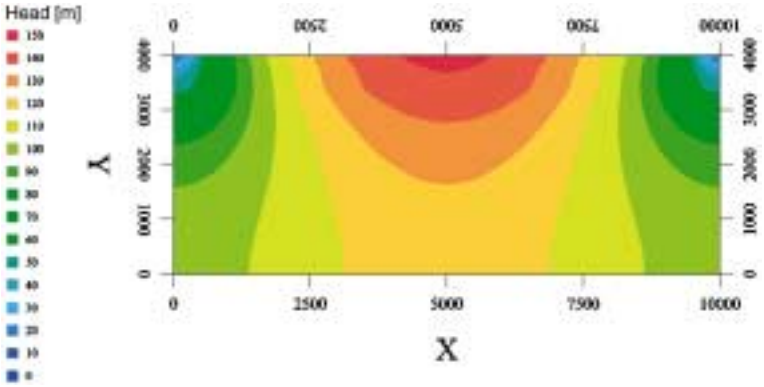

Figure A2 Cases 1 and 2: hydraulic head.

For the salt simulations (see Figures A3 to A5), the concentration evolution is five times faster in case 2 with variable porosity compared to case 1 with constant porosity. This observation is obtained when comparing Figures A4 and A5; these are almost identical at different times. These results are in accordance with the 3D results (cf chapter 4) showing an evolution of salinity, 5 to 10 time faster than simulation results of /Svensson, 1999/.

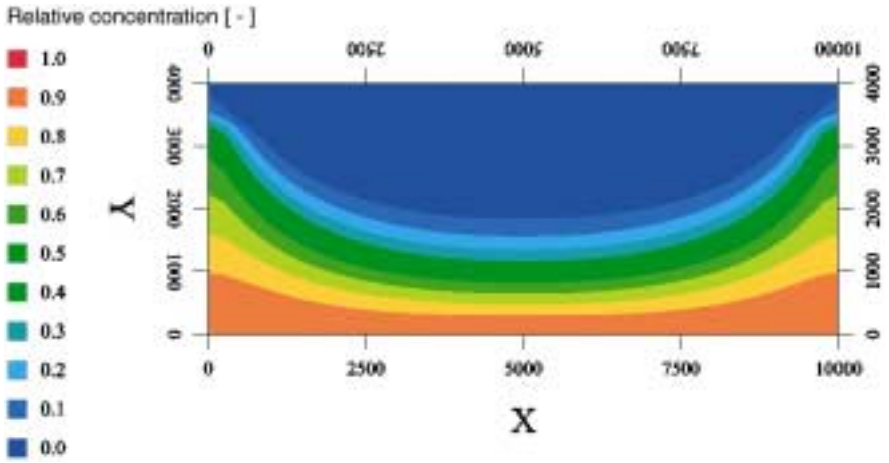

Figure A3 Case 1 (with constant porosity): salt concentration after 100 years.

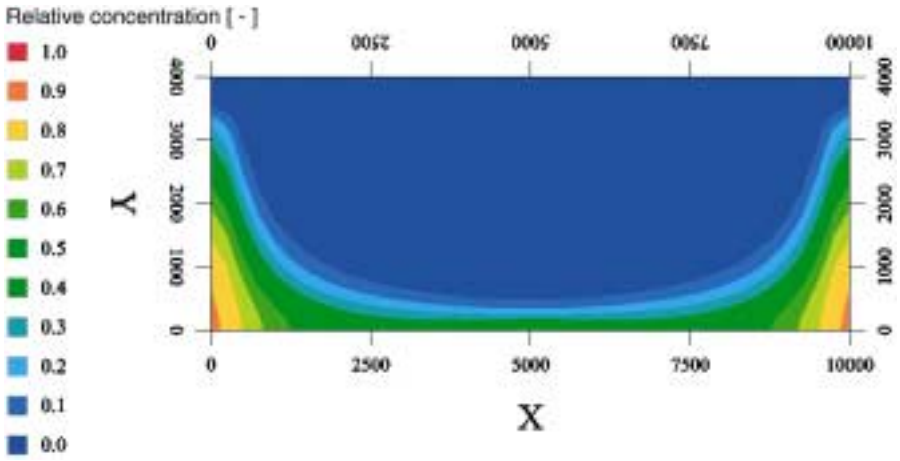

Figure A4 Case 1 (with constant porosity): salt concentration after 500 years.

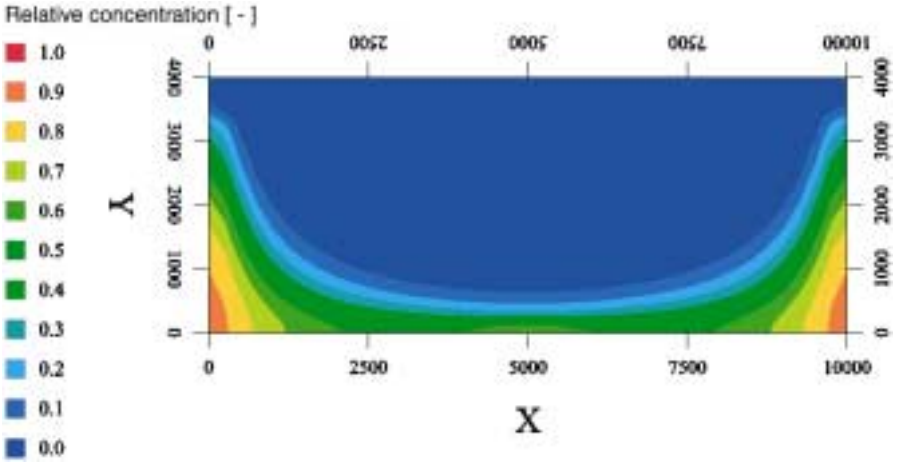

Figure A5 Case 2 (with variable porosity): salt concentration after 100 years.

Appendix B

INTEGRATION of NAMMU